Refractometry With a Tailored Sensitivity Based on a Single-Mode-Capillary-Single-Mode Fiber Structure

Xiaobei Zhang, *Member, IEEE*
Haiyang Shao
Yong Yang
Haiyang Pan
Fufei Pang
Tingyun Wang

Refractometry With a Tailored Sensitivity Based on a Single-Mode-Capillary-Single-Mode Fiber Structure
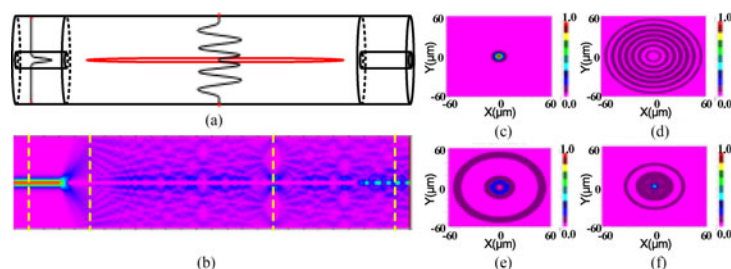
Xiaobei Zhang, *Member, IEEE*, Haiyang Shao, Yong Yang, Haiyang Pan, Fufei Pang, and Tingyun Wang

Laboratory of Specialty Fiber Optics and Optical Access Networks, School of
Communication and Information Engineering, Shanghai University, Shanghai 200072, China

Abstract: We demonstrate a simple structure for the refractive index sensing by splicing a segment of capillary with two segments of single-mode fibers (SMFs). By selecting appropriate splicing parameters, two mode coupling regions can be formed with tapered air-cavities on both sides of the capillary. This simple structure allows us the light propagation in the capillary with a ring mode distribution, while the high-order mode distributed in the capillary will be affected by the surrounding environment. With the inner diameter of the capillary increases, there is an enhancement of interaction between ring modes and the surrounding environment. Therefore, we can realize a tailored sensitivity based on the inner capillary diameter. Maximum refractive index sensitivities of 789, 1196, and 1684 nm/RIU can be obtained in the refractive index range from 1.3360 to 1.4365 when the inner diameter is 5, 15, and 25 μm, respectively. The distinguishing feature of such a capillary-based fiber sensor is that it can be used for the refractometry with a tailored high sensitivity through choosing the inner capillary diameter.

Index Terms: Optical fiber sensors, fiber optics, optical device fabrication.

1. Introduction

The fiber-based refractometry has the inherent advantages of fiber sensors such as the electromagnetic immunity, light weight, small size, resistance to harsh environments, and so on. To fabricate optical fiber refractive index (RI) sensor structures, various types of new structures and advanced processing technologies have been demonstrated, such as the trench-embedding fiber taper sensor fabricated by the laser pulse processing technology [1], [2], the normal photonic crystal fiber [3], the S-Tapered fiber sensor [4], the no-core fiber [5], the graphene-deposited photonic crystal fiber [6], and multimode microfiber [7]. As one of microstructure optical fiber, the hollow core fiber (HCF) also has been extensively studied [8]–[10]. A single mode fiber (SMF)-hollow core fiber-multimode fiber structure has been investigated and employed to realize the mode conversion [8]. A Mach-
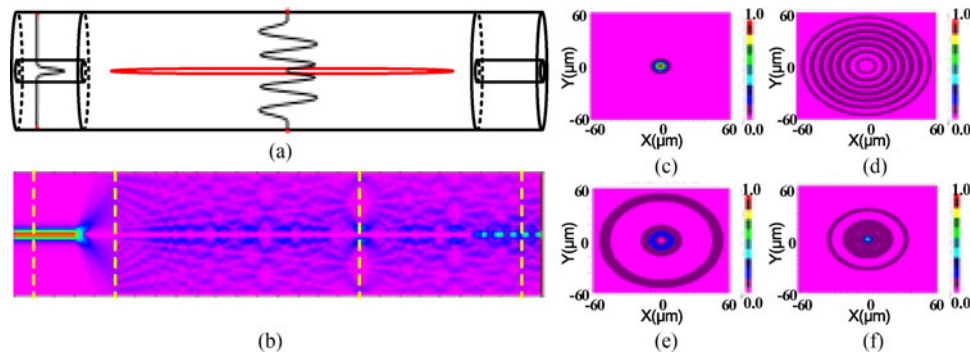
Fig. 1. (a). Scheme of the sensor structure, (b) the energy distribution of the sensor along the direction of light propagation, and the energy distribution on the cross sections when (c) $L = 500\,\mu$m, (d) $L = 2500\,\mu$m, (e) $L = 8500\,\mu$m, and (f) $L = 12500\,\mu$m.

Zehnder interferometer based on HCF was employed for the measurement of temperature and curvature simultaneously [9]. A Fabry–Perot interferometer based on special HCF was fabricated for photothermal gas sensor [10] and a Fabry–Perot interferometer based on a C-shaped hollow core fiber for RI sensing [11]. The capillary, as a special hollow core fiber, was used to develop a variety of micro-nano optics devices, such as the bandpass filter [12], ultracompact in-line broadband Mach-Zehnder interferometer [13], and in-Fiber Fabry–Perot and Mach-Zehnder interferometers [14]–[19]. There are also some sensor devices based on multimode interference that are proposed to achieve refractive index sensing, such as the tapered muticore fiber for magnetic field strength sensing [20], the multi-mode interferometer and FP composite structure based on the solid-core photonic crystal fiber and the hollow-core photonic crystal fiber for RI sensing [21]. Although some devices mentioned above can be used for sensing the refractive index, there are still some deficiencies, such as the complex laser fabrication [1], [2], tapering [4] processes, and the center offset induced poor robustness [14].

In this paper, we demonstrate a refractometry by splicing one section of capillary with two sections of single mode fiber (SMF) without any additional processing steps. RI sensing characteristics of such a sensor structure were studied by both simulation and experiment under various inner capillary diameters, with high sensitivities obtained.

2. Model and Theory

The capillary based sensor structure consists of one short segment of capillary spliced between two standard SMFs with appropriate splicing parameters. Fig. 1(a) shows the schematic diagram of this fiber device. Two mode coupling regions with tapered air-cavities on both sides of the capillary were formed after the splicing process. The mode coupling region can be regarded as a segment of multimode fiber with the core diameter of 120 μm and the cladding as the surrounding environment. The input light in the SMF has a fundamental mode field distribution. When the incident light reaches the coupling region, the input field will be coupled into eigenmodes LP_{0m} in the mode coupling region as in [22].

The modes in the coupling region propagate in the capillary and interfere with each other. The optical field of the capillary section can be calculated by

$$E(r) = \sum_{m=1}^{M} \alpha_m E_m(r) \exp(i\beta_m L) \tag{1}$$

where M is the count of cladding modes. α_m is the coupling coefficient from the LP_{01} mode in the SMF to the LP_{0m} mode in the capillary. $E_m(r)$ is the field distribution of the LP_{0m} mode in the capillary. β_m is the longitudinal propagation constant. L is the propagation length along the capillary. Therefore, the intensity distribution of the light field generated by the interference can be
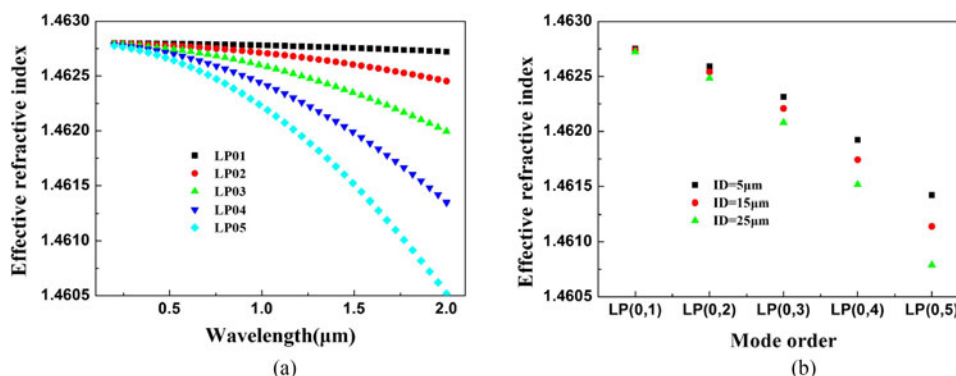
Fig. 2. Effective RI of eigenmodes in the capillary (a) with inner diameter of 5 μm varying with different wavelengths and (b) with different inner diameters at the wavelength at 1550 nm.

expressed as

$$I(r) = E(r)E^*(r) = \sum_{m=1}^{M}\sum_{n=1}^{M} \alpha_m \alpha_n^* E_m(r)E_n(r)\exp[i(\beta_m - \beta_n)L]. \tag{2}$$

When the condition satisfies $(\beta_m - \beta_n)L = 2N\pi$, the constructive interference occurs with N as an integer. Simulations are performed using a commercial Rsoft Beamprop module. Simulation parameters are as the following. The core and cladding RI of SMF are 1.4681 and 1.4628. The RI of capillary is same to the cladding RI of SMF. The capillary inner diameter (ID) is 5 μm. The length of the mode coupling region, the tapered air-cavity and the total device length are set as 150 μm, 200 μm and 10 mm, respectively. As shown in Fig. 1(b), the input fundamental mode field can be decomposed and coupled into the eigenmodes LP_{0m} when the light enters the mode coupling region.

For this capillary based sensor structure, we select four cross sections of the model to observe the energy distribution, as shown in Fig. 1(c)–(f). The modes coupled into the coupling region propagate in the capillary and interfere with each other. Therefore, the energy distribution of the cross section show different forms as L increases. Finally, the higher order modes coupling back to the core of SMF through another coupling region. The transmission spectrum of the capillary based sensor is obtained by interferences between different modes. We also calculate the effective refractive index of the capillary eigenmodes as shown in Fig. 2(a). The effective RI decreases with the mode order or the wavelength increasing. When the wavelength is fixed at 1550 nm, the larger inner capillary diameter is, the faster the rate of decrease in the effective RI with the mode order increasing, as shown in Fig. 2(b). The effective RI will be changed by the variation of the refractive index of the surrounding environment; hence, the longitudinal propagation constant β_m will be changed by the variation of the RI of the surrounding environment, resulting into the spectral wavelength shift for the sensing applications.

It can also be seen from Fig. 2(b) that the effective RI decreases when the inner diameter increases. The evanescent field of modes in the capillary increases as the inner diameter increases, so the RI sensitivity also increases, which will be confirmed in the following simulation and experimental results.

3. Device Fabrication and RI Sensing

To fabricate the proposed capillary based sensor, three types of quartz capillary from Ploymicro Technologies are used. The inner capillary diameters are 5 μm (TSP005150), 15 μm (TSP015150) and 25 μm (TSP025150), respectively. The outer diameter of all the capillaries is 150 μm. After removal of the polymer cladding, the outer diameter of all capillaries is 125 μm. First, a segment of capillary and a segment of single mode fiber (SMF28) were cleaved and spliced together by a

TABLE 1

Main Fusion Splicing Parameters in the Experiments

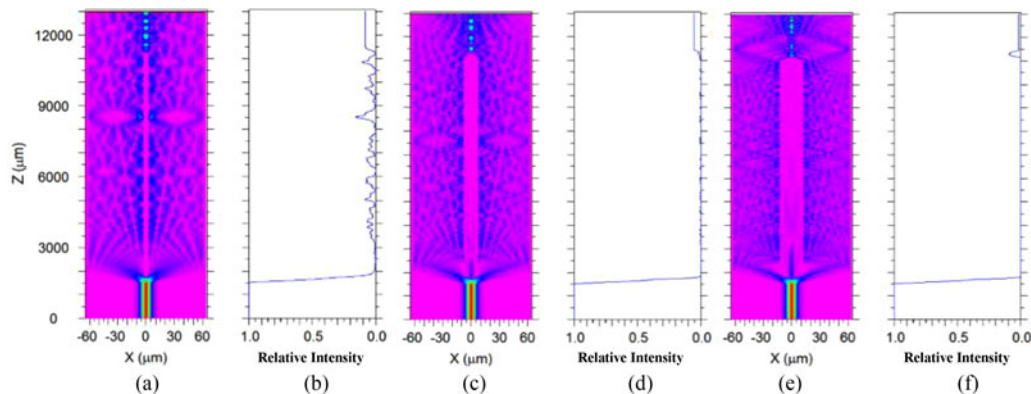| Parameters	Cleaning Arc	Gap	Overlap	Arc Power	Prefuse time	Fuse time
Data	20 ms	15 μm	20 μm	70 bit	100 ms	800 ms

Fig. 3. Different energy distribution in the device based on the capillaries with the inner capillary diameter as (a) 5 μm, (c) 15 μm, and (e) 25 μm. The output normalized optical power of the device with the inner capillary diameter as (b) 5 μm, (d) 15 μm, and (f) 25 μm.

commercial fusion splicer (FITEL-S178) with the rewritten splicing program. Table 1 lists the key parameters adopted in our experiments. Two mode coupling regions with tapered air-cavity on both sides of the capillary were formed after the two splicing steps, with the length of the mode coupling regions about 150 μm, and we cleave the capillary as a short section ($\sim$10 mm) connected with SMF. Finally, the other end of the capillary was fusion spliced with another SMF.

According to the above processing method, we fabricated three types of capillary based sensors with different inner diameters. All the sensors are about 10 mm long. At the same time, we established the appropriate numerical model. The main parameters of the numerical model are obtained from the fabricated devices, which is the same as Section 2. For the numerical simulation, the transmission spectra, insertion loss and the RI sensing characteristics of the sensors based on different capillaries are studied. The wavelength is set to 1550 nm. As shown in Fig. 3, the energy distribution and the output normalized optical power of the device are obtained. Through the normalized optical powers at the output port, the insertion loss increases as the inner diameter increasing for the wavelength at 1550 nm.

We also simulated the transmission spectra of all types of sensors from 1200 to 1700 nm with a step of 1 nm. The capillary inner diameter is 5, 15, and 25 μm. Then the transmission spectra were obtained as shown in the Fig. 4(a)–(c). Different transmission spectra correspond to the capillaries with different inner diameters. The greater the inner diameter is, the more intensive the energy distribution in the capillary cladding is. This leads to more complex pattern interferences and spectra. Experimentally, the transmission spectra are measured using an optical spectrum analyzer (Yokogawa, AQ6370B) with a resolution of 0.05 nm, and a wideband light source (SuperK COMPACT). The spectra of the sensors based on different capillaries are obtained as shown in the Fig. 4(d)–(f). As the inner diameter increases, the spectrum becomes more complex caused by the multiple interferences. As a relatively large inner diameter allows a small part light coupled into
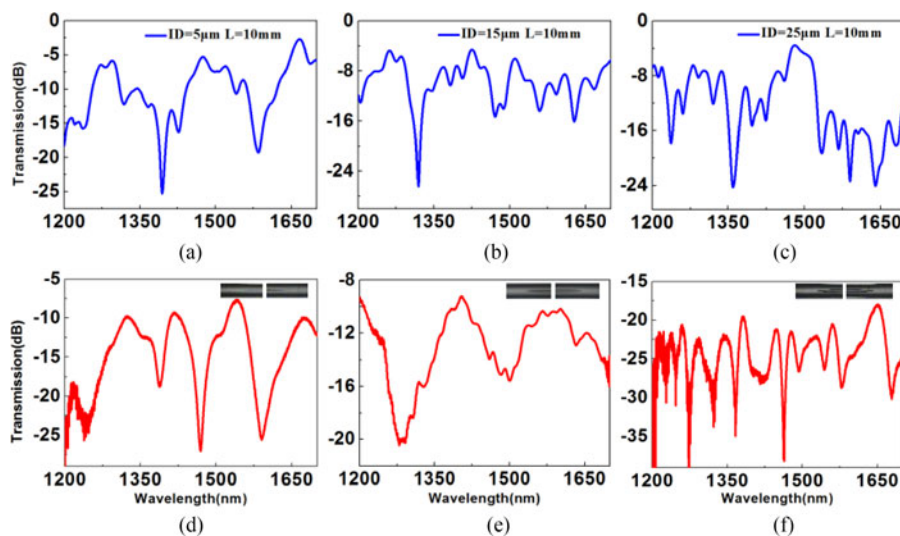
Fig. 4. Transmission spectra of the sensor. The simulations with the inner capillary diameter as (a) 5 μm, (b) 15 μm, and (c) 25 μm. The experiments with the inner capillary diameter as (d) 5 μm, (e) 15 μm, and (f) 25 μm. (insets) Microscope pictures of both sides of the device.
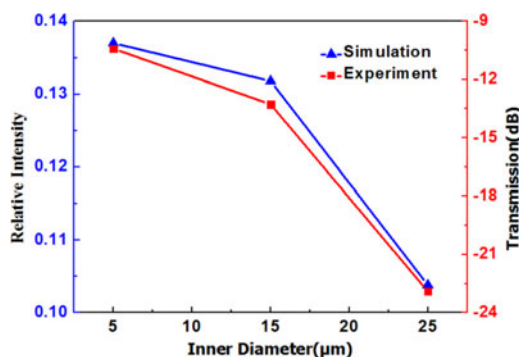

Fig. 5. Average transmission intensity of the simulation and experimental results.

the air core of the capillary, the complex spectrum for greater capillary diameter, as shown in Fig. 4(f), is due to two effects of the multimode interferences and the antiresonant reflection [23].

Comparing the simulation with the experimental results, the simulation results show the good agreement with the experimental results. The dip positions in the simulation spectra and the experimental spectra are not completely consistent, caused by the differences of the coupling region and tapered area between the numerical simulation model and experimental samples. Moreover, the experiment results are also affected by other factors, such as the temperature, the microbending and so on. We also calculated the average transmission intensity, which is the average of transmission intensities within the wavelengths from 1200 to 1700 nm. In both the simulation and experiment, the average transmission intensity decrease with the inner diameter increasing as shown in Fig. 5.

By clamping the fabricated device with two fiber holders, we investigated the surrounding refractive index response characteristics of the sensor from 1.3360 to 1.4521 at the room temperature. After each measurement, we clean the sensor with the ethanol to make the spectrum back to the initial spectrum. With the increasing of the RI, the spectrum will shift to the longer wavelength. The performance of the fabricated sensor based the capillary with inner diameter of 5 μm is tested firstly. The spectrum evolution is shown in the Fig. 6(a). The wavelength of the dip around 1468 nm is shown in Fig. 6(b). The maximum sensitivity is 4179 nm/RIU when the refractive index changes from 1.4472 to 1.4521. As the refractive index sensitivity is increasing when the inner diameter of
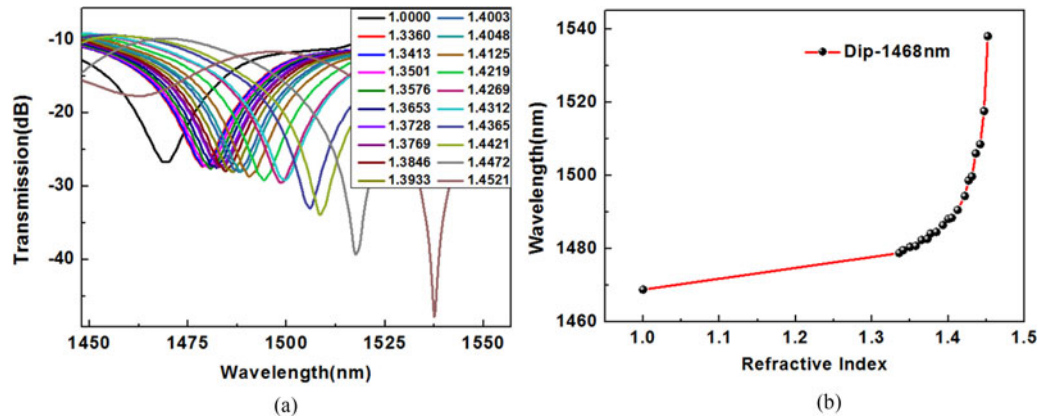
Fig. 6. (a) Spectral evolution with the RI increasing from 1.0 to 1.4512. (b) Wavelength of the dip around 1468 nm with the RI increasing.
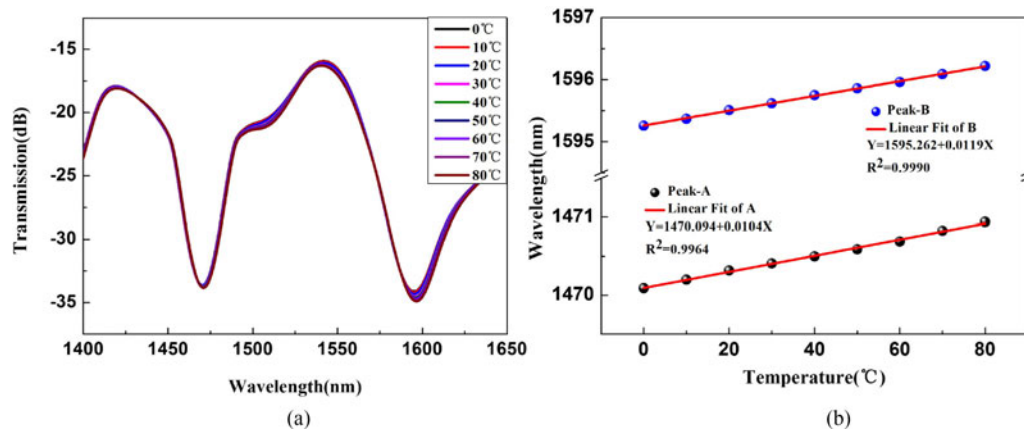

Fig. 7. (a) Spectral evolution with the temperature increasing from 0 °C to 80 °C. (b) Wavelength of the dip around 1468 nm and 1595 nm with the temperature increasing.

the capillary increases, the transmission spectrum is distorted when reaching a critical refractive index, and this critical refractive index will become smaller when the inner diameter increases. So we compare the characteristics of several capillaries based on different inner diameters in the range of 1.3360 to 1.4365. When the inner diameter is 5, 15 and 25 μm, respectively, maximum refractive index sensitivities of 789, 1196 and 1684 nm/RIU can be obtained in the refractive index range from 1.3360 to 1.4365.

The thermal stability of the device is very important for the refractive index sensing. Thus the temperature sensing experiment is also carried out with a device sample of which inner diameter is 5 μm. By monitoring the wavelength position of the dips to characterize the change of the ambient temperature. The spectrum evolution is shown in Fig. 7(a). The sensitivity of 10.4 pm/°C and 11.9 nm/°C when the wavelength of the dip around 1468 nm (peak A) and 1595 nm (peak B) are obtained, which is shown in Fig. 7(b). The results show that the temperature sensor sensitivity is around 10 pm/°C, which is due to the intrinsic property of the capillary material. When the temperature is nearly stabled during the experiment, the temperature-induced cross-sensing effect can be ignored.

According to the above process, the RI sensing performance of those sensors based on the capillaries with different inner diameters is tested respectively. Simultaneously, we calculate the evolution of the sensor transmission spectra by changing the RI of the background of the numerical simulation model, and we analyze the data obtained from the RI sensing simulation and
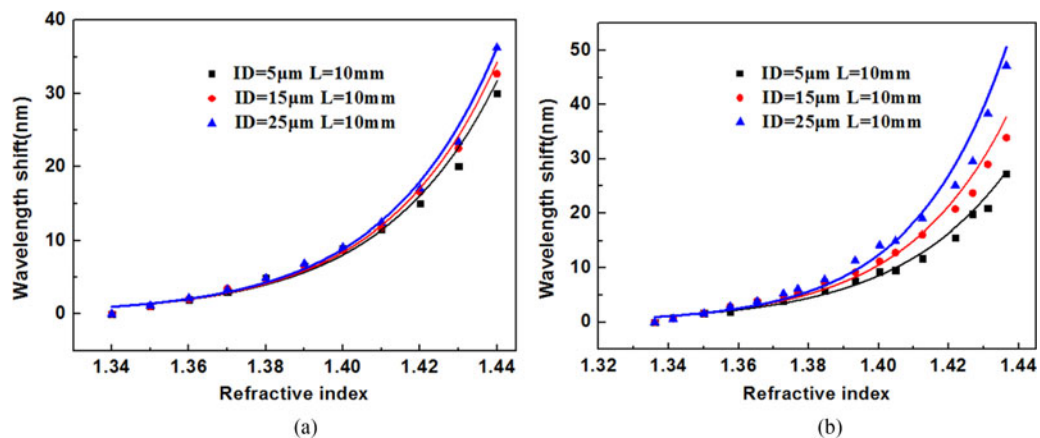
Fig. 8. Relationship between wavelength shift distance and the refractive index in the (a) simulation. (b) Experiment.
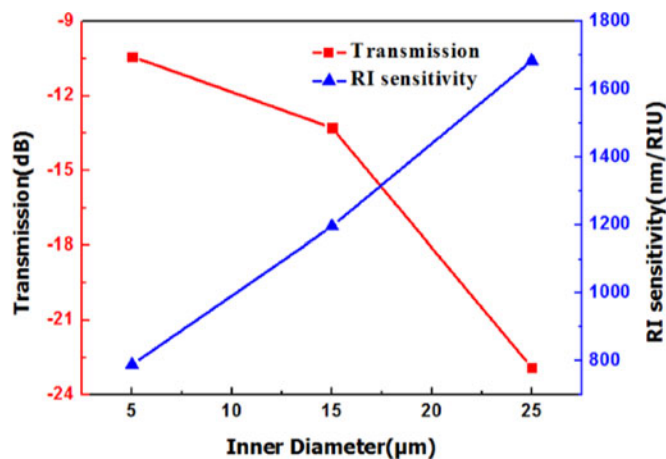

Fig. 9. Average transmission intensity and the refractive index sensitivity of the experimental results.

experiments. Fig. 8(a) shows the RI sensing simulation, we can easily obtained that the wavelength shift distance of all sensor models show exponential relationship with the RI, and with the RI increasing, the RI sensitivity significantly increased. Similarly, the experimental results as shown in Fig. 8(b) are also consistent with the above conclusions. As shown in Fig. 8(a) and (b), the RI sensitivity is increasing with the inner diameter increases. When the inner diameter is increasing from 5 to 25 μm, the RI sensitivity is proportional to the inner capillary diameter.

The average insertion loss and the maximum refractive index sensitivity increases when the inner diameter increases, as shown in Fig. 9. The average insertion loss and the sensitivity is a trade-off in the practical design of RI sensors. Therefore we can obtain a higher sensitivity by using the capillary with the diameter greater than 25 μm to a certain extent. However, the sensitivity cannot unlimitedly increase, as the sensor cannot be used for the refractive index sensing anymore when the insertion loss is large.

4. Conclusion

In this work, a refractometry was demonstrated by splicing a segment of capillary with two segments of standard SMF with appropriate splicing parameters. We investigated the mechanism of light transmission in the device and the RI sensing characteristic of the sensor structure. Maximum refractive index sensitivities of 789, 1196 and 1684 nm/RIU can be obtained in the refractive index

range from 1.3360 to 1.4365 when the inner diameter is 5, 15, and 25 μm, respectively. Improved RI sensitivities could be achieved experimentally using larger inner diameter. This device has the advantages of simple structure, easy fabrication process, low cost and high sensing sensitivity. Besides, this structure gives controllable parameter (capillary inner diameter) to improve the sensitivity. This device structure has great potentials for applications in the bio-sensing, concentration, and chemical gas detections.

References

[1] Z. Cao, L. Jiang, S. Wang, P. Wang, F. Zhang, and Y. Lu, "Trench-embedding fiber taper sensor fabricated by a femtosecond laser for gas refractive index sensing," *Appl. Opt.*, vol. 53, no. 6, pp. 1028–1032, Feb. 2014.

[2] R. M. André *et al.*, "Simultaneous measurement of temperature and refractive index using focused ion beam milled Fabry-Perot cavities in optical fiber micro-tips," *Opt. Exp.*, vol. 24, no. 13, pp. 14053–14065, Jun. 2016.

[3] R. Jha, J. Villatoro, G. Badenes, and V. Pruneri, "Refractometry based on a photonic crystal fiber interferometer," *Opt. Lett.*, vol. 34, no. 5, pp. 617–619, Mar. 2009.

[4] R. Yang *et al.*, "S-Tapered fiber sensors for highly sensitive measurement of refractive index and axial strain," *IEEE J. Lightw. Technol.*, vol. 30, no. 19, pp. 3126–3132, Oct. 2012.

[5] J. Zhao *et al.*, "Refractive index fiber laser sensor by using tunable filter based on no-core fiber," *IEEE Photon. J.*, vol. 8, no. 5, pp. 1–8, Oct. 2016.

[6] Y. C. Tan, Z. Q. Tou, K. K. Chow, and C. C. Chan, "Graphene-deposited photonic crystal fibers for continuous refractive index sensing applications," *Opt. Exp.*, vol. 23, no. 24, pp. 31286–31294, Nov. 2015.

[7] H. Luo *et al.*, "Refractive index sensitivity characteristics near the dispersion turning point of the multimode microfiber-based Mach-Zehnder interferometer," *Opt. Lett.*, vol. 40, no. 21, pp. 5042–5045, Nov. 2015.

[8] S. Choi, K. Oh, W. Shin, and U. C. Ryu, "Low loss mode converter based on adiabatically tapered hollow optical fibre," *Electron. Lett.*, vol. 37, no. 13, pp. 823–825, Jun. 2001.

[9] Y. Zhang, A. Zhou, B. Qin, and Q. Xu, "Simultaneous measurement of temperature and curvature based on hollow annular core fiber," *IEEE Photon. Technol. Lett.*, vol. 26, no. 11, pp. 1128–1131, Jun. 2014.

[10] F. Yang, Y. Tan, W. Jin, Y. Lin, Y. Qi, and H. L. Ho, "Hollow-core fiber Fabry-Perot photothermal gas sensor," *Opt. Lett.*, vol. 41, no. 13, pp. 3025–3028, Jul. 2016.

[11] C. Wu, Z. Liu, A. P. Zhang, B. O. Guan, and H. Y. Tam, "In-line open-cavity Fabry-Pérot interferometer formed by C-shaped fiber fortemperature-insensitive refractive index sensing," *Opt. Exp.*, vol. 22, no. 18, Sep. 2014, Art. no. 21757.

[12] S. Choi, T. J. Eom, Y. Jung, B. H. Lee, J. W. Lee, and K. Oh, "Broad-band tunable all-fiber bandpass filter based on hollow optical fiber and long-period grating pair," *IEEE Photon. Technol. Lett.*, vol. 17, no. 1, pp. 115–117, Jan. 2005.

[13] Y. Jung, S. Lee, B. H. Lee, and K. Oh, "Ultracompact in-line broadband Mach-Zehnder interferometer using a composite leaky hollow-optical-fiber waveguide," *Opt. Lett.*, vol. 33, no. 24, pp. 2934–2936, Dec. 2008.

[14] D. W. Duan *et al.*, "In-fiber Fabry-Perot and Mach-Zehnder interferometers based on hollow optical fiber fabricated by arc fusion splicing with small lateral offsets," *Opt. Commun.*, vol. 284, no. 22, pp. 5311–5314, Jul. 2011.

[15] C. L. Lee, H. Y. Ho, J. H. Gu, T. Y. Yeh, and C. H. Tseng, "Dual hollow core fiber-based Fabry-Perot interferometer for measuring the thermo-optic coefficients of liquids," *Opt. Lett.*, vol. 40, no. 4, pp. 459–462, Feb. 2015.

[16] B. Xu, C. Wang, D. N. Wang, Y. Liu, and Y. Li, "Fiber-tip gas pressure sensor based on dual capillaries," *Opt. Exp.*, vol. 23, no. 18, pp. 23484–23492, Sep. 2015.

[17] G. K. Costa *et al.*, "In-fiber fabry-perot interferometer for strain and magnetic field sensing," *Opt. Exp.*, vol. 24, no. 13, pp. 14690–14696, Jun. 2016.

[18] S. Pevec and D. Donlagic, "Multiparameter fiber-optic sensor for simultaneous measurement of thermal conductivity, pressure, refractive index, and temperature," *IEEE Photon. J.*, vol. 9, no. 1, pp. 1–14, Feb. 2017.

[19] M. Hou, F. Zhu, Y. Wang, Y. Wang, C. Liao, S. Liu, and P. Lu, "Antiresonant reflecting guidance mechanism in hollow-core fiber for gas pressure sensing," *Opt. Exp.*, vol. 24, no. 24, pp. 27890–27898, Nov. 2016.

[20] E. Tagoudi, K. Milenko, and S. Pissadakis, "Intercore coupling effects in multicore optical fiber tapers using magnetic fluid out-claddings," *IEEE J. Lightw. Technol.*, vol. 34, no. 23, pp. 5561–5565, Dec. 2016.

[21] J. N. Dash and R. Jha, "Fabry-Perot based strain insensitive photonic crystal fiber modal interferometer for inline sensing of refractive index and temperature," *Appl. Opt.*, vol. 54, no. 35, pp. 10479–10486, Dec. 2015.

[22] Q. Wu, Y. Semenova, P. Wang, and G. Farrell, "High sensitivity SMS fiber structure based refractometer-analysis and experiment," *Opt. Exp.*, vol. 19, no. 9, pp. 7937–7944, Mar. 2011.

[23] P. Rugeland, C. Sterner, and W. Margulis, "Visible light guidance in silica capillaries by antiresonant reflection," *Opt. Exp.*, vol. 21, no. 24, pp. 29217–29222, Dec. 2013.